Published in final edited form as:
Cancer Res. 2011 October 1; 71(19): 6116–6121. doi:10.1158/0008-5472.CAN-10-4557.

Effects of photoacoustic imaging and photothermal ablation therapy mediated by targeted hollow gold nanospheres in an orthotopic mouse xenograft model of glioma

Wei Lu[1,#], **Marites P. Melancon**[1,2], **Chiyi Xiong**[1], **Qian Huang**[1], **Andrew Elliott**[2], **Shaoli Song**[1], **Rui Zhang**[1], **Leo G. Flores II**[1], **Juri G. Gelovani**[1], **Lihong V. Wang**[3], **Geng Ku**[1], **R. Jason Stafford**[2], and **Chun Li**[1,*]

[1]Department of Experimental Diagnostic Imaging, The University of Texas MD Anderson Cancer Center, Houston, Texas [2]Department of Imaging Physics, The University of Texas MD Anderson Cancer Center, Houston, Texas, and [3]Department of Optical Imaging Laboratory, Department of Biomedical Engineering, Washington University, St. Louis, Missouri

Abstract

Advancements in nanotechnology have made it possible to create multifunctional nanostructures that can be used simultaneously to image and treat cancers. For example, hollow gold nanospheres (HAuNS) have been shown to generate intense photoacoustic signals and induce efficient photothermal ablation (PTA) therapy. In this study, we used photoacoustic tomography (PAT), a hybrid imaging modality, to assess the intravenous delivery of HAuNS targeted to integrins that are overexpressed in both glioma and angiogenic blood vessels in a mouse model of glioma. Mice were then treated with near-infrared laser, which elevated tumor temperature by 20.7 °C. We found that PTA treatment significantly prolonged the survival of tumor-bearing mice. Taken together, these results demonstrate the feasibility of using a single nanostructure for image-guided local tumor PTA therapy using photoacoustic molecular imaging.

Introduction

With nanotechnology, it is possible to create multifunctional nanostructures capable of mediating diagnostic imaging, treatment, and monitoring of therapeutic response. For example, pegylated gold nanorods were used for both X-ray computed tomography and photothermal ablation (PTA) (1). This approach sometimes referred to as “theranostics”, holds a great promise for cancer diagnosis and therapy. Photoacoustic tomography (PAT) is a hybrid imaging modality that detects absorbed photons ultrasonically through the photoacoustic effect (2). PAT is capable of detecting optical contrast agents with high sensitivity and specificity (3-5). With the metal nanocomposites, photoacoustic imaging and temperature measurement for photothermal cancer therapy was investigated in tissue-mimicking phantoms and excised animal tissues (6).

We hypothesize that PAT is an accurate and sensitive imaging modality for cancer diagnosis and for assessing targeted delivery to brain tumors of gold nanostructures used for PTA therapy. Silica-cored gold nanoshells, which are under clinical investigation, have been

[*]**Corresponding author**: Department of Experimental Diagnostic Imaging, Unit 59, The University of Texas MD Anderson Cancer Center, 1515 Holcombe Boulevard, Houston, Texas 77030. Phone: (713) 792-5182. Fax: (713) 794-5456. cli@mdanderson.org..
[#]**Present address:** Department of Biomedical and Pharmaceutical Sciences, College of Pharmacy, The University of Rhode Island, Kingston, Rhode Island.

shown to mediate effective PTA therapy and improve survival in a murine glioma model (7). In this work, we demonstrated that intravenous injection of hollow gold nanospheres (HAuNS) targeted to integrins that are overexpressed in both glioma and angiogenic blood vessels (4, 8, 9), permitted PAT of orthotopically inoculated U87 glioma in nude mice and mediated selective antitumor effect when mice were irradiated with near-infrared (NIR) laser. Although there have been numerous reports on theranostic applications of cancer nanotechnology, to the best of our knowledge, this is the first report to demonstrate simultaneous molecular PAT and PTA therapy for cancer with a single platform of targeted nanoparticles.

Materials and Methods

Nanoparticle synthesis

HAuNS were synthesized as previously described (10). Cyclic RGD peptide c(KRGDf) was synthesized manually using PL-DMA resin and N^{α}-Fmoc chemistry (11). Cyclic RGD peptides have been used for imaging and treatment of glioma (4, 8, 9) because of their high binding affinity to integrin receptors such as $\alpha_v\beta_3$ receptors (IC_{50}=2-40 nM) (12, 13). The peptide was conjugated to one terminus of a heterodifunctional poly(ethylene glycol) (PEG) precursor, *N*-hydroxysuccinimidyl-PEG-*S*-acetylthioacetate (NHS-PEG-SATA; molecular weight 5,000), through its ε-amine of lysine residue and activated ester in NHS-PEG-SATA. The sulfhydryl group on the other terminus of c(KRGDf)-PEG-SATA was released by treatment with 0.5 M hydroxylamine in PBS (Supplementary Fig. S1). HAuNS (8.5×10^{12} particles/mL) were then added to argon-purged aqueous solution containing c(KRGDf)-PEG-SH (50 μg/mL) and PEG-SH (500 μg/mL, Sigma) and the solution was stirred overnight at room temperature to give c(KRGDf)-PEG-HAuNS (Fig. 1A). PEG-SH was conjugated to HAuNS similarly to give PEG-HAuNS (nonspecific control).

Photoacoustic imaging

PAT of mouse brain inoculated with human glioblastoma stably transfected with *luciferase* gene (U87-TGL) was carried out as we previously described (3). A brief description of the PAT technique is provided in the supplemental information. The cell line provided by Dr. Juri G. Gelovani (University of Texas) in January 2008 was validated by STR DNA fingerprinting by the Characterized Cell Line Core Facility at UT MD Anderson Cancer Center on April 12, 2011. The STR profiles were compared to known ATCC fingerprints, and to the Cell Line Integrated Molecular Authentication database (CLIMA) version 0.1.200808 (http://bioinformatics.istge.it/clima/). The STR profiles matched known DNA fingerprints of U87-MG.

On day 8 after tumor inoculation, mice were imaged using a prototype PAT scanner. Mice were then injected intravenously with c(KRGDf)-PEG-HAuNS or PEG-HAuNS (2.5×10^{11} particles per mouse). Contrast-enhanced photoacoustic images were acquired 24 h after nanoparticle injection. Imaging data were reconstructed using modified delay and sum back-projection reconstruction algorithm. After data acquisition, mice were sacrificed by overexposure to CO_2. Open-skull surgery was performed to permit photography of the brain tumors.

Micro-positron emission tomography (μPET)

To further confirm the accuracy of PAT imaging of U87 tumors, c(KRGDf)-PEG-HAuNS were labeled with the positron emitter ^{64}Cu ($t_{1/2}$=12.7 h) (14). Tumor-bearing mice were injected intravenously with ^{64}Cu-labeled c(KRGDf)-PEG-HAuNS or ^{64}Cu-labeled PEG-HAuNS at a dose of 7.5 mCi/kg (n=3 per agent). Twenty-four hours later, mice were anesthetized with 2% isoflurane (Baxter). Mice were subjected to a 7-min micro-computed

tomography (μCT) scan followed by a 20-min μPET scan using an Inveon μPET/CT Scanner (Siemens). The μPET/CT images were generated separately and then fused using Inveon Research Workplace version 3.0 (Siemens).

Photothermal therapy

On day 8 after tumor inoculation, mice were injected intravenously with D-luciferin (4 mg/kg) for bioluminescence imaging. Mice were randomly allocated into five groups of 15 mice each. Groups I and IV were injected intravenously with c(KRGDf)-PEG-HAuNS, group II with PEG-HAuNS (both 2.5×10^{11} particles per mouse), and groups III and V with saline. Groups I-III were also treated with NIR laser irradiation (16 W/cm^2, 3 min, 808 nm) 24 h after nanoparticle injection. In each group, 5 mice were subjected to luciferase bioluminescence imaging at various times after nanoparticle injection to measure tumor burden (response to PTA therapy), and 10 mice were subjected to survival monitoring. Survival data were presented using Kaplan-Meier plots and analyzed using a log-rank test. $P < 0.05$ was considered statistically significant.

Results

PAT permits visualization of U87 gliomas in intact nude mice

Transmission electron microscopy showed that c(KRGDf)-PEG-HAuNS were spherical, had hollow interiors, had average diameter of ~40 nm, and had an absorption peak tuned to ~800 nm (Fig. 1B). We previously demonstrated that the molar extinction coefficient associated with the optical absorption cross-section of HAuNS (1.4×10^{11} $M^{-1}\cdot cm^{-1}$) is much higher than that of hemoglobin ($\sim1\times10^3$ $M^{-1}\cdot cm^{-1}$). Indeed, PEG-HAuNS at a concentration as low as 20 pM displayed the same optical absorption as hemoglobin at its typical blood concentration of 2.3 mM (3). The strong absorption of PEG-HAuNS in the NIR region permitted intense contrast in PAT.

Images of mice with U87 glioma before and after intravenous injection of c(KRGDf)-PEG-HAuNS or PEG-HAuNS are shown in Figure 1C. Precontrast PAT only showed the normal brain vasculature. There was a low signal-to-background ratio between tumor and normal brain with no significant difference in photoacoustic (PA) signal intensities (Fig. 1D). However, 24 h after injection of c(KRGDf)-PEG-HAuNS, PAT clearly revealed brain tumor, and the tumor location on PAT correlated with mouse brain anatomy. Quantitative analysis confirmed that the mean contrast-enhanced PA signal ratio of tumor-to-contralateral normal brain 24 h after c(KRGDf)-PEG-HAuNS injection was about twice as high as that obtained from precontrast images (p=0.0375). In contrast, 24 h after injection of PEG-HAuNS, there was no change in tumor-to-brain PA ratio compared to that obtained from precontrast PAT images (p=0.4677). These data supported that selective accumulation of c(KRGDf)-PEG-HAuNS enhanced PAT of U87 glioma.

μPET/CT confirms accuracy of PAT imaging of U87 gliomas with c(KRGDf)-PEG-HAuNS

At 24 h after intravenous injection, ^{64}Cu-labeled c(KRGDf)-PEG-HAuNS showed 2.9-fold higher uptake than ^{64}Cu-labeled PEG-HAuNS in U87 tumors (1.12±0.22%ID/g versus 0.38±0.12%ID/g, Fig. 2 and Supplementary Fig. S2), and autoradiography showed higher radioactivity in tumor with c(KRGDf)-PEG-HAuNS than PEG-HAuNS. In addition to integrin $\alpha_v\beta_3$, recent study showed that c(KRGDf) may also interact with other integrins such as $\alpha_v\beta_5$ (15). Here, we used immunohistochemical staining of integrin $\alpha_v\beta_3$ receptors in tumors to confirm HAuNS localization. The intracranial distribution of radioactivity matched well with the site of tumor inoculation as well as the distribution of integrin $\alpha_v\beta_3$. Selective uptake of c(KRGDf)-PEG-HAuNS in U87 tumors was further supported by

microscopy, which revealed greater accumulation of c(KRGDf)-PEG-HAuNS than PEG-HAuNS in tumors (Fig. 2).

Injection of c(KRGDf)-PEG-HAuNS plus NIR laser irradiation elevates temperature of U87 gliomas

Representative magnetic resonance temperature imaging (MRTI) maps of mouse brains at the end of laser irradiation are shown in Fig. 3A. Dynamic temperature curves based on MRTI analysis revealed that NIR laser irradiation in mice injected with c(KRGDf)-PEG-HAuNS reached a maximum temperature of 57.75 ± 0.46 °C (Fig. 3B), which is above the threshold of temperature of 54°C needed for irreversible cell damage (16, 17). In contrast, NIR laser irradiation in mice injected with nontargeted PEG-HAuNS or saline resulted in maximum temperatures of 48.14 ± 0.12 °C and 41.65 ± 0.09 °C, respectively, which were insufficient to induce irreversible cell damage (Fig. 3B).

PTA therapy with c(KRGDf)-PEG-HAuNS prolongs survival of mice with orthotopic U87 gliomas

Bioluminescence imaging showed significantly decreased luminescence intensity in tumors of mice treated with c(KRGDf)-PEG-HAuNS injection and laser irradiation (Fig. 4A and 4B). This tumor-ablation effect was observed during the first 9 days after laser treatment (days 9-17), when the luminescence intensity was lower than that before laser treatment (day 8). On day 19 and later, the luminescence intensity exceeded that before laser treatment, indicating brain tumor recurrence. In mice treated with PEG-HAuNS plus laser, luminescence intensity in tumors decreased only on day 9. In mice treated with laser alone, c(KRGDf)-PEG-HAuNS alone, or saline, luminescence intensity increased throughout treatment.

The median survival time of mice treated with c(KRGDf)-PEG-HAuNS plus laser (28 d) was significantly longer than that of the other groups ($P < 0.001$): PEG-HAuNS plus laser, 19.5 d; laser alone, 17.5 d; c(KRGDf)-PEG-HAuNS alone, 17.5 d; and saline, 16.5 d (Fig. 4C). Histologic examination confirmed that c(KRGDf)-PEG-HAuNS plus laser was the treatment causing the most extensive necrotic response (Fig. 4D). Extensive pyknosis, cytoplasmic acidophilia (10, 17), and corruption of the extracellular matrix of the tumor appeared throughout tumors of mice treated with c(KRGDf)-PEG-HAuNS plus laser. The tumor cells were completely ablated; there were no discernible residue viable tumor cells in the tumor periphery (Fig. 4D, arrow). In mice treated with PEG-HAuNS plus laser or laser alone, about 45% and 30% of tumor tissues were necrotized, characterized as pyknosis and medium cytoplasmic acidophilia, and there were large numbers of viable tumor cells in the periphery (Fig. 4D, asterisks). In tumors of mice treated with c(KRGDf)-PEG-HAuNS alone or saline alone, most tumor cells were intact.

Discussion

We have demonstrated effective PAT imaging and PTA therapy of glioma mediated by a single preparation of targeted HAuNS based on their intrinsically high optical absorption cross-section. The findings from our current study suggest potential applications of HAuNS as a novel theranostic platform. First, c(KRGDf)-PEG-HAuNS can serve as efficient optical contrast agents for photoacoustic imaging, which may provide cancer diagnosis with high-resolution and high-sensitivity in addition to conventional imaging modalities. The PAT may also be useful for pretreatment diagnosis, real-time monitoring of treatment, as well as assessment of treatment outcome. Second, under the guidance of PAT imaging, accurate and efficient PTA of tumor cells would be instituted simply by switching the laser power from diagnostic level (pulsed laser, 50 mW/cm^2) to therapeutic level (diode laser, 16 W/cm^2) on

the basis of the high photothermal coupling efficiency of HAuNS. Third, given that μPET/CT using ^{64}Cu-labeled c(KRGDf)-PEG-HAuNS confirmed selective uptake of the nanoparticles in U87 tumors, PET/CT with ^{64}Cu-labeled targeted HAuNS should provide alternative imaging method for HAuNS mediated PTA therapy.

With these advantages, we envision that for treating an entire tumor volume, delivery of laser energy to the region of interest would be achieved in a way similar to that of interstitial high-dose rate brachytherapy in that multiple applicators are used to cover the area of interest (18). For small recurrent tumors, which are a large and important patient population, this would provide a minimally invasive technique to both diagnose and target the recurrence using a single fiber. Remaining PAT signal from the tumor bed or beyond after surgery could guide further resection and/or provide opportunity for selective ablation mediated by the targeted HAuNS. If successfully implemented in the clinical setting, our approach described here offer an alternative option over current clinical investigations of glioma theranostics involving CT-guided thermotherapy with superparamagnetic iron-oxide nanoparticles in an alternating magnetic field (19, 20). In this case, the nanoparticles are administered intratumorally under neuronavigational control and pretreatment MRI.

Although no viable tumor cells were found on histologic evaluation after treatment with c(KRGDf)-PEG-HAuNS plus NIR irradiation, we did observe regrowth of tumor, suggesting the presence of residual tumor cells after treatment. Combining PTA therapy and other treatment modalities, such as photothermal chemotherapy made possible with drug-loaded HAuNS or photothermal transfection made possible with HAuNS coated with therapeutic siRNA (14), should lead to further enhanced therapeutic outcome and even cure. Studies towards this goal are currently under way.

Supplementary Material

Refer to Web version on PubMed Central for supplementary material.

Acknowledgments

We thank Stephanie Deming for editing the manuscript.

Grant support: This work was supported in part by grants from the National Institutes of Health (grant R01 CA119387 05 S1 and MD Anderson's Cancer Center Support Grant CA016672), the John S. Dunn Foundation, SPORE Head and Neck Career Development Award P50CA097007 (to M.P.M), and an Odyssey Fellowship (to M.P.M.). Funding as an Odyssey Fellow is supported by the Odyssey Program and The Cockrell Foundation Award for Scientific Achievement at the University of Texas M. D. Anderson Cancer Center. The ^{64}Cu was provided by Washington University Medical School, which is partially funded by National Cancer Institute grant R24 CA86307.

References

1. von Maltzahn G, Park JH, Agrawal A, et al. Computationally guided photothermal tumor therapy using long-circulating gold nanorod antennas. Cancer Res. 2009; 69:3892–3900. [PubMed: 19366797]
2. Wang X, Pang Y, Ku G, Xie X, Stoica G, Wang LV. Noninvasive laser-induced photoacoustic tomography for structural and functional in vivo imaging of the brain. Nat Biotechnol. 2003; 21:803–806. [PubMed: 12808463]
3. Lu W, Huang Q, Ku G, et al. Photoacoustic imaging of living mouse brain vasculature using hollow gold nanospheres. Biomaterials. 2010; 31:2617–2626. [PubMed: 20036000]
4. De la Zerda A, Zavaleta C, Keren S, et al. Carbon nanotubes as photoacoustic molecular imaging agents in living mice. Nat Nanotechnol. 2008; 3:557–562. [PubMed: 18772918]

5. Kim JW, Galanzha EI, Shashkov EV, Moon HM, Zharov VP. Golden carbon nanotubes as multimodal photoacoustic and photothermal high-contrast molecular agents. Nat Nanotechnol. 2009; 4:688–694. [PubMed: 19809462]
6. Shah J, Park S, Aglyamov S, et al. Photoacoustic imaging and temperature measurement for photothermal cancer therapy. J Biomed Opt. 2008; 13:034024. [PubMed: 18601569]
7. Day ES, Thompson PA, Zhang L, et al. Nanoshell-mediated photothermal therapy improves survival in a murine glioma model. J Neurooncol. 2010 in press (DOI 10.1007/s11060-11010-10470-11068).
8. Reardon DA, Fink KL, Mikkelsen T, et al. Randomized phase II study of cilengitide, an integrin-targeting arginine-glycine-aspartic acid peptide, in recurrent glioblastoma multiforme. J Clin Oncol. 2008; 26:5610–5617. [PubMed: 18981465]
9. Lee HY, Li Z, Chen K, et al. PET/MRI dual-modality tumor imaging using arginine-glycine-aspartic (RGD)-conjugated radiolabeled iron oxide nanoparticles. J Nucl Med. 2008; 49:1371–1379. [PubMed: 18632815]
10. Lu W, Xiong C, Zhang G, et al. Targeted photothermal ablation of murine melanomas with melanocyte-stimulating hormone analog-conjugated hollow gold nanospheres. Clin Cancer Res. 2009; 15:876–886. [PubMed: 19188158]
11. Wang W, Wu Q, Pasuelo M, McMurray JS, Li C. Probing for integrin alpha v beta3 binding of RGD peptides using fluorescence polarization. Bioconjug Chem. 2005; 16:729–734. [PubMed: 15898744]
12. Haubner R, Wester HJ, Reuning U, et al. Radiolabeled alpha(v)beta3 integrin antagonists: a new class of tracers for tumor targeting. J Nucl Med. 1999; 40:1061–1071. [PubMed: 10452325]
13. Haubner R, Wester HJ, Burkhart F, et al. Glycosylated RGD-containing peptides: tracer for tumor targeting and angiogenesis imaging with improved biokinetics. J Nucl Med. 2001; 42:326–336. [PubMed: 11216533]
14. Lu W, Zhang G, Zhang R, et al. Tumor site-specific silencing of NF-kappaB p65 by targeted hollow gold nanosphere-mediated photothermal transfection. Cancer Res. 2010; 70:3177–3188. [PubMed: 20388791]
15. Zannetti A, Del Vecchio S, Iommelli F, et al. Imaging of alpha(v)beta(3) expression by a bifunctional chimeric RGD peptide not cross-reacting with alpha(v)beta(5). Clin Cancer Res. 2009; 15:5224–5233. [PubMed: 19671851]
16. Sapareto SA, Dewey WC. Thermal dose determination in cancer therapy. Int J Radiat Oncol Biol Phys. 1984; 10:787–800. [PubMed: 6547421]
17. Chen J, Glaus C, Laforest R, et al. Gold nanocages as photothermal transducers for cancer treatment. Small. 2010; 6:811–817. [PubMed: 20225187]
18. Tselis N, Kolotas C, Birn G, et al. CT-guided interstitial HDR brachytherapy for recurrent glioblastoma multiforme. Long-term results. Strahlenther Onkol. 2007; 183:563–570. [PubMed: 17896088]
19. Maier-Hauff K, Rothe R, Scholz R, et al. Intracranial thermotherapy using magnetic nanoparticles combined with external beam radiotherapy: results of a feasibility study on patients with glioblastoma multiforme. J Neurooncol. 2007; 81:53–60. [PubMed: 16773216]
20. Maier-Hauff K, Ulrich F, Nestler D, et al. Efficacy and safety of intratumoral thermotherapy using magnetic iron-oxide nanoparticles combined with external beam radiotherapy on patients with recurrent glioblastoma multiforme. J Neurooncol. 2011; 103:317–324. [PubMed: 20845061]

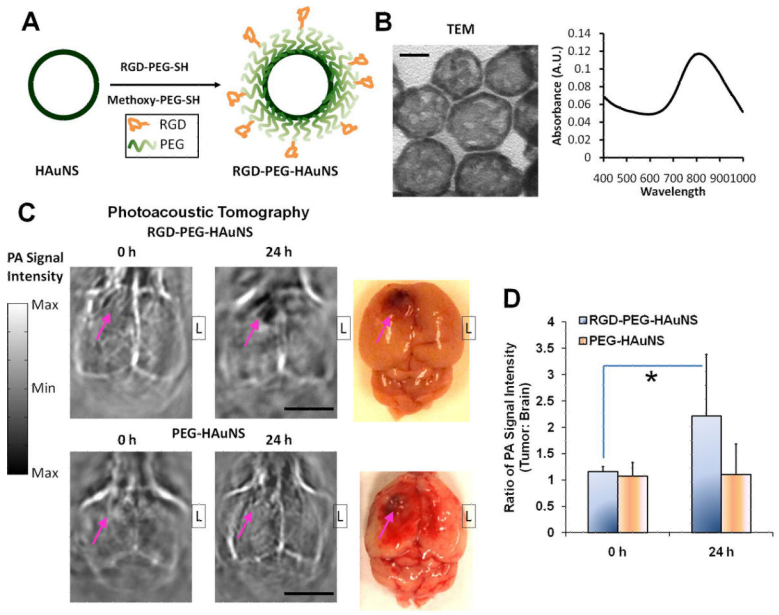

Figure 1.

A, scheme for c(KRGDf)-PEG-HAuNS bioconjugation. *B*, c(KRGDf)-PEG-HAuNS characteristics on transmission electron microscopy (bar, 20 nm) and UV-Vis spectrum (measured in water). *C*, PAT images of U87 human glioma in mouse brains before (0 h) and 24 h after intravenous injection of nanoparticles (bar, 5 mm). Photographs of corresponding mouse brains were used to confirm tumor location. Arrows, locations of tumors; L, left. *D*, PA signal intensity ratio of tumor-to-contralateral brain in mice before (0 h) and 24 h after injection of HAuNS. Data are presented as mean ± SD. c(KRGDf)-PEG-HAuNS group, n=5; PEG-HAuNS group, n=4. * indicates significant difference between precontrast and 24 h postcontrast groups ($p<0.05$).

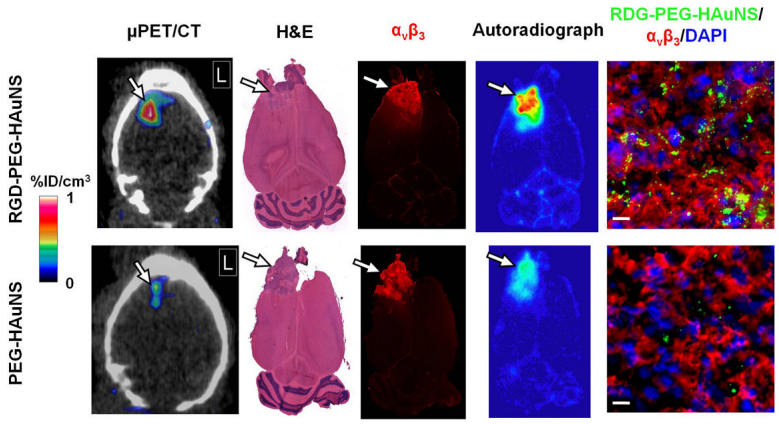

Figure 2.

Targeted delivery of ^{64}Cu-labeled c(KRGDf)-PEG-HAuNS to U87 human glioma in mouse brains. Shown are μPET/CT images (obtained 24 h after intravenous injection of nanoparticles); photographs of mouse brains stained with hematoxylin-eosin and $\alpha_v\beta_3$ and autoradiographs of mouse brains; and immunofluorescence micrographs of tumor tissue at high magnification. Red, $\alpha_v\beta_3$; green, scattering signal of HAuNS under dark field; blue, DAPI-stained cell nuclei; arrows, tumors; bar, 10 μm.

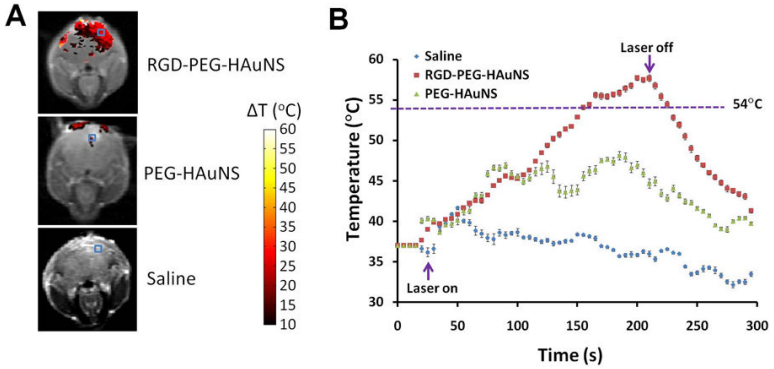

Figure 3.

Real-time MRTI of U87 human gliomas in mouse brains 24 h after injection of HAuNS. *A*, overlap of mouse brain T1-weighted MRI with Magnevist and MRTI at the end of laser irradiation. *B*, tumor temperature change versus time in the region of interest (blue rectangles in Fig. 3A). Laser (16 W/cm^2 at 808 nm) was applied for 3 min between the time points indicated by the arrows.

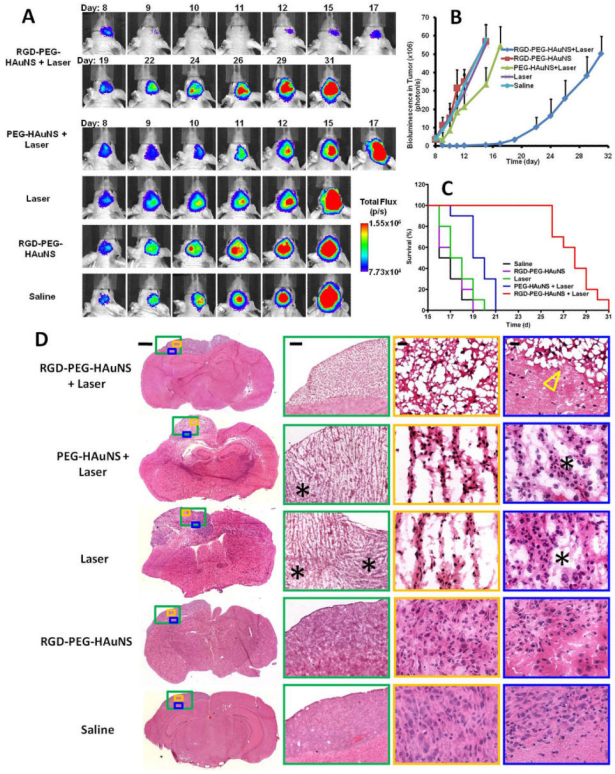

Figure 4.

Photothermal ablation of U87 human gliomas in mouse brains. *A*, representative bioluminescence images of nude mice bearing U87-TGL tumors with different treatments (see Materials and Methods). *B*, quantitative analysis of bioluminescence beginning with treatment administration on day 8 after tumor inoculation (n=5 per group). *C*, Kaplan-Meier survival curve of tumor-bearing mice treated as in B (n=10 per group). *D*, histologic evaluation of tumor necrosis. Left lane, representative photographs of tumor-bearing mouse brains stained with hematoxylineosin 24 h after NIR laser irradiation. Right three lanes, representative microphotographs at high magnification of the areas corresponding to the boxed areas in the left lane. Arrow indicates no discernible residual viable tumor cells in the tumor periphery. Asterisks indicate viable tumor cells in mice treated with PEG-HAuNS plus laser or laser alone. Bars (left to right), 1 mm, 200 μm, 20 μm, 20 μm.